High order modes of intense second harmonic light produced from a plasma aperture

E. Bacon,[1] M. King,[1,2] R. Wilson,[1] T. P. Frazer,[1] R. J. Gray,[1] and P. McKenna[1,2,a)]
[1)] *SUPA Department of Physics, University of Strathclyde, Glasgow G4 0NG, United Kingdom*
[2)] *The Cockcroft Institute, Sci-Tech Daresbury, Warrington WA4 4AD, United Kingdom*

(Dated: 25 June 2022)

Due to their ability to sustain extremely high amplitude electromagnetic fields and transient density and field profiles, plasma optical components are being developed to amplify, compress and condition high power laser pulses. We recently demonstrated the potential to use a relativistic plasma aperture, produced during the interaction of a high power laser pulse with an ultrathin foil target, to tailor the spatio-temporal properties of intense fundamental and second harmonic light generated [Duff *et al.*, Scientific Reports **10**, 105 (2020)]. Here, we numerically explore the interaction of an intense laser pulse with a preformed aperture target to generate second harmonic laser light with higher-order spatial modes. The maximum generation efficiency is found for aperture diameter close to the full width at half maximum of the laser focus and for target thickness on the micron-scale. The spatial mode generated is shown to depend strongly on the polarisation of the drive laser pulse, which enables changing between a linearly polarised TEM_{01} and a circularly polarised Laguerre–Gaussian, LG_{01}, mode. This demonstrates the use of a plasma aperture to generate intense, higher frequency light with selectable spatial mode structure.

I. INTRODUCTION

The ability to manipulate light at relativistic intensities[1] ($> 10^{18}$ Wcm^{-2} for a laser wavelength of $\sim$1 μm) is an important aspect of the development of compact laser-driven particle and radiation sources[2,3]. Such sources have wide ranging potential applications including medicine[4–6], ultrafast imaging[7], industrial processing[8] and inertial confinement fusion[9,10]. Tailoring the spatial and temporal profile of the laser pulse can be used to optimise focusing behaviour in laser-plasma interactions[11], which can enhance laser-driven particle acceleration[12,13], and has the potential to produce radiation sources with orbital angular momentum[14].

The conventional approach to manipulating light is based on the use of solid state optical media, but there is a limit to the energy density that this media can withstand before nonlinear effects distort the laser pulse and the optic itself is damaged. This is typically circumvented by increasing the size of the optic as the laser energy is increased, so that the overall energy density is below the critical value. However, large area optics are very expensive, with long manufacture times and limited manoeuvrability due to their volume and weight. Plasma optical components by contrast are inherently compact, easily achieving energy densities of more than two orders of magnitude higher. In addition, the ultrafast evolution of the optical properties of laser-excited plasma enables other properties of the laser pulse to be tailored. Through the use of plasma-based optics, it is possible to enhance the temporal-intensity contrast of the laser pulse[15–17], refocus the laser pulse to significantly enhance the laser peak intensity[18–20], compress the laser pulse temporal profile[21], generate high harmonics[22–24] and amplify the pulse[25–27]. Through the interaction of intense light with dense plasma oscillations, the production of transient plasma gratings[28–30], holograms[31] and coherent emission of light[32] can also be achieved.

In recent studies, involving intense laser pulse interactions with ultrathin (tens-of-nanometre) foils, we introduced the concept of a self-generated *relativistic plasma aperture* that enables the laser light to pass through a region of an initially opaque target, resulting in diffraction and manipulation of the particle dynamics in the corresponding field structures[33,34]. This plasma aperture forms due to a region of the target becoming relativistically transparent[35] to the laser light, which occurs when the plasma frequency ω_p ($= \sqrt{n_e e^2/(\gamma \epsilon_0 m_e)}$, where n_e is the electron density, e is the electron charge, γ is the electron Lorentz factor, ϵ_0 is the permittivity of free space and m_e is the electron rest mass) is reduced to a value lower than the laser frequency, ω_L. The electron density at which this occurs is known as the relativistically corrected critical density, γn_{crit}, and at currently achievable laser intensities, the process is aided by target heating and expansion reducing the peak electron density in the focal spot region. As relativistic induced transparency occurs above an intensity threshold, the spatial profile for a Gaussian focal spot is circular, forming a relativistic plasma aperture in the target[33]. As the transmitted portion of the laser pulse interacts with the edge of this plasma aperture, intense light is generated at ω_L and $2\omega_L$ with higher order transverse spatial mode structures and different polarisation states compared with the drive laser pulse[36]. An example result from a 3D particle-in-cell (PIC) simulation of the interaction of an intense pulse with an initially solid density 10 nm-thick aluminium target is shown in figure 1(a), in

[a)] Electronic mail: paul.mckenna@strath.ac.uk

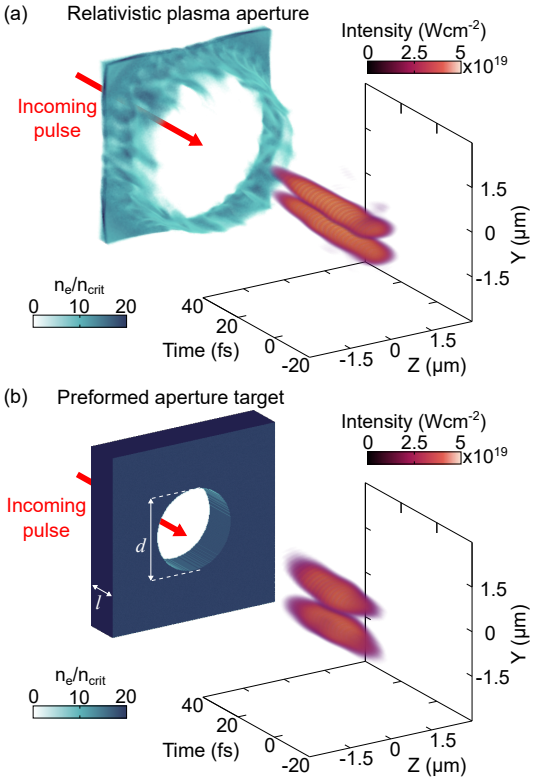

FIG. 1. Example 3D simulation results demonstrating the generation of relativistically-intense frequency-doubled light in a higher-order spatial mode (TEM_{01}), driven by intense laser light in a fundamental TEM_{00} mode, from: (a) a self-generated relativistic plasma aperture in an initially solid density 10 nm-thick aluminium target; (b) a preformed aperture target with thickness l=2 μm and aperture diameter d=3 μm.

which the self-generated relativistic plasma aperture and $2\omega_L$ light, emitted in the TEM_{01} mode, are observed. This was driven by a linearly-polarised (in Y), 6 J, 40 fs-duration laser pulse focused to a peak intensity equal to 6×10^{20} Wcm^{-2}, in a fundamental TEM_{00} mode. See Duff *et al.*[36] for a fuller description of the high order spatial mode generation mechanism. When the incoming laser light is circularly polarised, light with orbital angular momentum (OAM) can be produced at the higher harmonics of the laser frequency[37].

The laser-plasma aperture interaction effectively acts to transfer energy from the incoming laser pulse, which has a fundamental Gaussian spatial mode structure, to intense harmonic light in higher order modes. This could potentially be developed as a plasma optics device. Although the use of ultrathin targets is challenging due to their fragility that can limit shot repetition rate, the scheme could potentially be simplified through the use of micron-thick targets incorporating a preformed circular aperture to produce the same effect[36]. This is illustrated in figure 1(b), which is an example 3D simulation result (parameters given further below) showing the generation of relativistically intense $2\omega_L$ light, in the TEM_{01} mode, in a target with thickness l=2 μm and aperture diameter d=3 μm. These targets could then also be used as a platform to more readily test the underlying physics that occurs during the formation of a relativistic plasma aperture.

In this article, we investigate the potential use of preformed aperture targets for the generation of frequency doubled light with higher order spatial mode structures. We determine the optimum target parameters to maximise the efficiency of energy transfer, using 2D and 3D PIC simulations. We show that this is related to the fraction of light transmitted through the aperture, the strength of the longitudinal electric field at the aperture circumference and the absorption of the laser pulse. Using 3D simulations, we compare the generation efficiency and mode structure formation when the polarisation is varied from linear to circular. The results highlight the feasibility of using a preformed aperture target, resulting in a plasma aperture, as a type of plasma optical device for mode conversion of intense light.

II. METHODS

To investigate and optimise the generation of frequency doubled light in higher order spatial modes, 2D and 3D simulations were performed using the fully relativistic PIC code EPOCH[38]. For the 2D case, the simulation XY grid was defined as 1000 × 720 mesh cells, corresponding to 20 μm × 20 μm. For the 3D simulations, the XYZ grid was defined as 1000 × 720 × 720 cells, corresponding to 20 μm × 20 μm × 20 μm. The targets were composed of a slab of Al^{13+} ions of thickness, l, with a circular aperture of diameter, d. This was neutralised with an electron population with a peak density equal to $30n_{crit}$ and an initial temperature of 10 keV. Each species was initialised with an average of 80 particles per cell in the 2D case and 5 particles per cell in the 3D. The boundaries of the simulation box were all defined as free-space and the ions were mobile in all cases.

The pulse of laser light with wavelength λ_L=800 nm entering from the left, X, boundary in both the 2D and 3D simulations and was focused at the plane corresponding to the front surface of the target, X=0. Both the laser pulse temporal and spatial profiles were defined, in terms of intensity, as Gaussian with the pulse duration, τ_L=40 fs (full width at half maximum; FWHM) and focal spot diameter ϕ_L=2.1 μm (FWHM). Time t=0 was defined as corresponding to the peak of the pulse reaching the front surface of the target i.e. the front of the aperture. In 3D, simulations using linear polarisation in the Y direction and circular polarisation were performed. In 2D, only linear polarisation in the Y direction was used because circular polarisation cannot interact with the full aperture surface. The peak laser pulse intensity, I_L, was varied from 10^{21} Wcm^{-2} to 10^{23} Wcm^{-2} by increasing the energy in the pulse.

A simulation automation code called BISHOP[39], de-

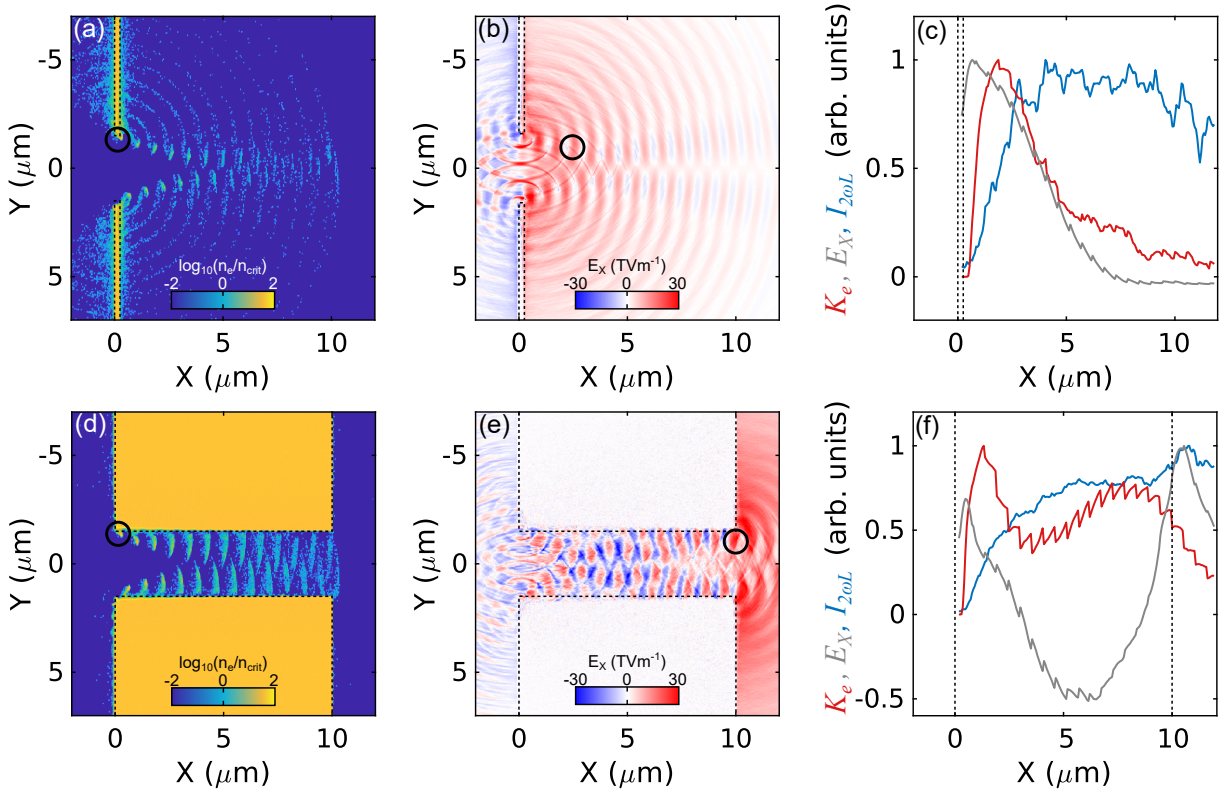

FIG. 2. Top: 2D simulation results for a $l = 0.5$ μm and $d = 3$ μm target: (a) electron density at $t = -4.8$ fs; (b) longitudinal electric field at $t = 2.8$ fs; (c) total energy (K_e, red) in the electron bunch marked by the black circle in (a) and (b) as it propagates in space, together with the intensity of the $2\omega_L$ light generated, averaged 400 nm around the bunch ($I_{2\omega L}$, blue) and the longitudinal electric field experienced by the bunch (E_X, grey) averaged over the same area. Bottom (d)-(f): Corresponding plots for $l = 10$ μm and $d = 3$ μm, with (e) at $t = 28.8$ fs. The dashed black lines indicate the initial positions of the target surfaces.

veloped by our group, was used to systematically scan a 2D parameter grid of target thickness and aperture diameter in 2D simulations. l was varied from 0.5 μm to 10 μm and d was varied from 0.5 μm to 5 μm.

III. RESULTS

A. 2D Simulations

Figure 2(a) shows the electron density for a $l = 0.5$ μm target at $t = -4.8$ fs from a 2D simulation, demonstrating the generation of electron bunches from the predefined ($d = 3$ μm) aperture edges as the laser interacts and propagates through. At each side, the electron bunches are emitted with frequency ω_L, π out of phase with the opposite side (due to the oscillation of the laser electric field vector), with an overall frequency equal to $2\omega_L$ when considering the bunches from both sides of the aperture. An example 2D map of the longitudinal electric field, 6 fs afterwards, is shown in figure 2(b). The pattern is produced by the interference from the two point sources at the opposite edges of the aperture. To investigate the temporal generation of $2\omega_L$ light generation, an arbitrary electron bunch, circled in figure 2(a), with it corresponding position shown 6 fs later in figure 2(b), is tracked through the simulation. The total kinetic energy in the bunch, K_e, is plotted together with the generated $2\omega_L$ intensity, $I_{2\omega L}$ and longitudinal electric field experienced, E_X, (both averaged 400 nm around the bunch) as a function of X (the axis of laser propagation) in figure 2(c). The electron bunch is immediately accelerated to relativistic velocities from the aperture edge, before experiencing a decelerating longitudinal electric field as it propagates with the laser and into the sheath field at the target rear (formed due to the charge separation of earlier fast electrons and rear surface plasma surrounding the aperture[40,41]). This can be observed as the overall positive electric field (in the $+X$ direction) at the rear of the target, together with the longitudinal field associated with the laser pulse, in figure 2(b). Both the acceleration and deceleration of the electron bunch results in broadband emission that constructively interferes with the emission from neighbouring bunches, resulting in the generation of $2\omega_L$ light. This is due to the periodic nature of the accelerated bunches produced at either side of the aperture, which have an overall frequency equal to $2\omega_L$. As a result of this, the intensity of the $2\omega_L$ light

along the longitudinal axis increases with distance from the aperture for about 5 μm, after which it saturates and then reduces as the generated $2\omega_L$ light expands away out from the sampled region in the vicinity of the bunch.

Figure 2(d)-(f) shows the corresponding results for the case $l = 10$ μm ($d = 3$ μm), for which the aperture effectively becomes a channel. In this case, figure 2(e) shows the longitudinal electric field 24 fs after the electron density plot in figure 2(d), when the bunch has reached the rear of the target. As can be seen in figure 2(f), the initial acceleration of the electron bunch and generation of $2\omega_L$ light is similar to the $l = 0.5$ μm case. However, as the electron bunch and laser co-propagate within the extended plasma aperture/channel, the electrons experience the positive longitudinal field associated with the focused Gaussian pulse (due to the divergence of the laser electric field profile i.e. $\nabla \cdot \vec{E} = 0$ in free space), resulting in a deceleration of the bunch. The overall bunch velocity never reduces to zero and it continues to propagate in the positive X direction with a relativistic velocity at all times. As the bunch propagates, it begins to dephase with the laser pulse and experiences the negative longitudinal field associated with the subsequent half-wave period, accelerating the bunch again. In both the deceleration and acceleration phases, the electrons emit, and the constructive interference with the neighbouring emission produces a strong $2\omega_L$ signal. As the bunch leaves the aperture/channel at $X = 10$ μm, it experiences the sheath field at the target rear and again decelerates, resulting in further $2\omega_L$ emission.

The aperture diameter and target thickness influence the energy conversion to $2\omega_L$. To determine the influence of these parameters, a detailed parameter scan was performed to observe the changes to the generation efficiency, based on the ratio of the total energy of the generated $2\omega_L$ light detected 5 μm from the target rear to the energy of the input laser pulse. Figure 3 shows the conversion efficiency as a function of target thickness and aperture diameter for three different laser intensities. For $I_L = 10^{21}$ Wcm^{-2}, the optimal efficiency is found to be $d \sim 2$ μm, shown in figure 3(a) as region I. At this aperture diameter, the efficiency saturates for $l \gtrsim 6$ μm. When the aperture diameter is increased, the edges of the aperture experience less interaction with the longitudinal field of the laser pulse and the efficiency of $2\omega_L$ thus reduces, as observed in region II.

Region III indicated that for small d, the efficiency decreases with increasing l. This is due to poor matching conditions between the free-space Gaussian laser beam focus and the close-to-cut-off modes that can exist within the aperture when the thickness is increased beyond the wavelength. This acts to attenuate the beam within the aperture. As d is reduced from the optimal at 2 μm (for the 2.1 μm FWHM laser focal spot), the generation efficiency therefore becomes very dependent on l. For the thickest targets, the efficiency reduces to negligible levels because the beam is greatly attenuated. However, reducing l enables appreciable efficiency to be regained, as indicated by region IV. This is due to the aperture evolving with the laser pulse. While small apertures inhibit the propagation of laser light due to poor matching conditions, the transverse ponderomotive force of the focused light is intense enough to expel the plasma from the focal spot region. If the target is thin enough, this expulsion is enough to increase the size of the aperture and continue to generate $2\omega_L$ light, similar to that of the interaction with an ultrathin foil target as reported by Duff *et* al.[36]. This effect can be more readily observed as the peak intensity is increased. At $I_L = 10^{22}$ Wcm^{-2}, shown in figure 3(b), the generation efficiency for the smallest d occurs over a much larger l range, and region IV becomes wider in the 2D parameter map. As the intensity is increased further, to $I_L = 10^{23}$ Wcm^{-2}, as shown in figure 3(c), region IV becomes broad across the entire d and l ranges, resulting in no observable region III. This effect is likely to be exaggerated by the reduced peak density (in comparison to solid density $\sim$430 n_{crit}) used in the simulations. In this scenario, I_L is high enough at the edges of the aperture that the heating of the plasma by the laser is sufficient for the interaction region to become relativistically transparent near the peak of the pulse, regardless of d. This acts to reduce the efficiency of the generation mechanism as the effective aperture diameter is now much larger than the starting value, in all cases. The optimal condition at $d \sim 2$ μm still exists because the rising edge of the laser pulse (with less intensity) still interacts with the initial aperture diameter.

B. Efficiency modelling

We next explore the observed dependence of the $2\omega_L$ generation efficiency on d and l. It is shown above that during the interaction of the laser pulse with the aperture circumference, the longitudinal electric field acts to accelerate and decelerate the bunched electrons. It is therefore assumed that the magnitude of the field close to the aperture circumference plays a role in defining the efficiency of $2\omega_L$ generation. The longitudinal electric field for a pulse with a focused Gaussian spatial profile can be determined from the spatial differential of the electric field along the polarisation direction. The absolute of this field maximises at a transverse position of Y$\sim \phi_L/2$. As such, as the d is increased, the magnitude of this longitudinal electric field at the aperture circumference, E_X, is maximised when $d \sim \phi_L$. This is shown in figure 4(a). The definition for a pulse linearly polarised in the Y dimension is given as:

$$E_X(Y) = \frac{d}{dY} e^{-(\frac{2\sqrt{ln(2)}Y}{\phi_L})^2} \quad (1)$$

The fraction of the laser light that can enter the aperture is another factor that influences $2\omega_L$ generation. The greater the energy that can propagate through the

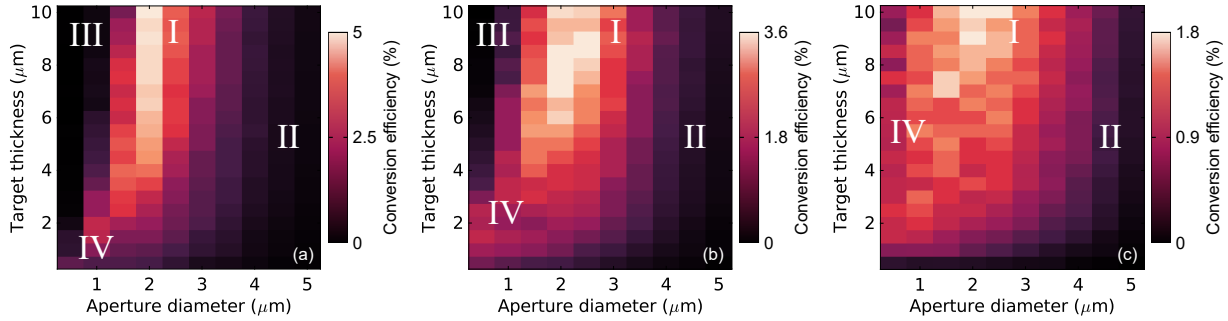

FIG. 3. 2D simulation results showing the efficiency of $2\omega_L$ light generation as a function of target thickness and aperture diameter, after the interaction of a linearly polarised laser pulse with intensity equal to: (a) 10^{21} Wcm^{-2}, (b) 10^{22} Wcm^{-2} and (c) 10^{23} Wcm^{-2}. All other laser parameters are fixed. The regions of behaviour indicated by the Roman numerals and discussed in the main text.

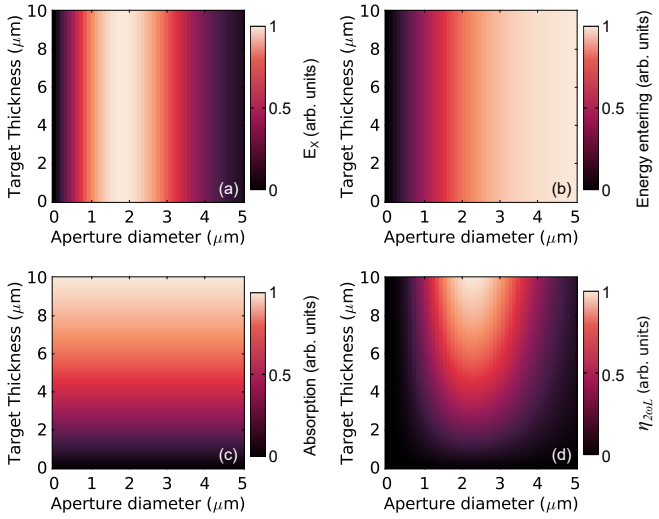

FIG. 4. Three parameters that vary with both target thickness and aperture diameter, for the interaction with a 10^{21} Wcm^{-2} laser pulse: (a) magnitude of the longitudinal electric field at the aperture circumference; (b) energy into the aperture; and (c) laser absorption. (d) Conversion efficiency to $2\omega_L$, as defined by equation 4.

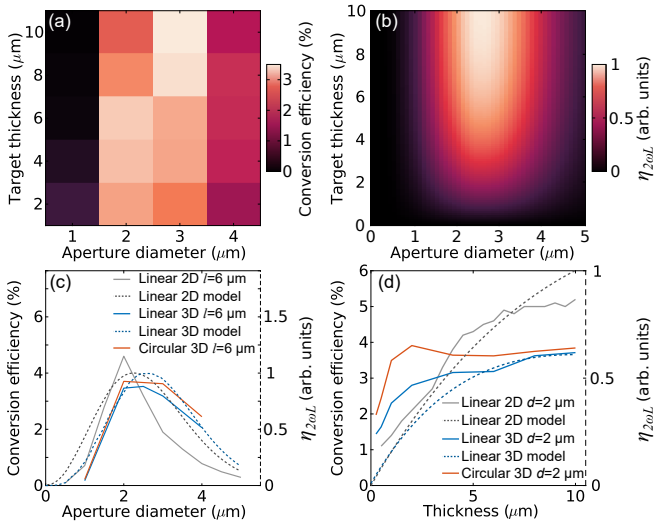

FIG. 5. 3D simulation results. (a) $2\omega_L$ generation efficiency as a function of d and l. (b) Conversion efficiency as given by equation 4 for 3D conditions. $2\omega_L$ generation efficiency: (c) as a function of d for l=6 μm; and, (d) as a function of l for d=3 μm. 3D linear polarisation results are shown in blue and circular polarisation results are shown in orange. 2D simulation data is included for comparison (dashed black line) for fixed l=6 μm and d=2 μm in (c) and (d), respectively. $I_L = 10^{21}$ Wcm^{-2} in all cases.

aperture, the greater the potential conversion into second harmonic light. The energy in the pulse that can enter the aperture, K_{in}, is shown in figure 4(b) for the 2D simulations, and given by:

$$K_{in}(d) = \int_{-d/2}^{d/2} e^{-(\frac{2\sqrt{ln(2)}Y}{\phi_L})^2} dY \qquad (2)$$

This varies with d, as more of the laser pulse is blocked for smaller apertures. Although as I_L is increased, relativistic transparency at the aperture edges can occur, enabling more light to enter, this is a second order effect and is not included in this simple model.

A third parameter influencing conversion to $2\omega_L$ light is the overall absorption of the energy of the laser pulse into the electron bunches, Abs_L, as it propagates through the aperture. We assume this varies linearly with l with an absorption coefficient, α, because the number of electrons exposed to the propagating laser pulse increases with l. We also assume an exponential attenuation of the laser pulse with thickness with an attenuation constant β. As the actual attenuation of the laser pulse is complicated by effects such as self-focusing and reflection, the attenuation constant is treated as a free parameter, approximated based on the level of transmitted light in the simulation results (β=0.1). This is shown in figure 4(c) and the overall absorption is given as:

$$Abs_L(l) = \alpha l e^{-\beta l} \qquad (3)$$

Assuming a linear relation between each of these pa-

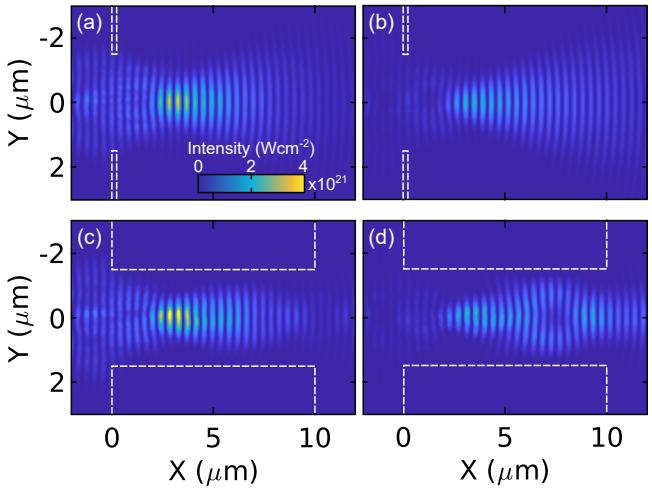

FIG. 6. Top: Intensity profile of the drive laser light in the $X-Y$ plane at Z=0 μm, from 3D simulations, for d=3 μm and l=0.25 μm at: (a) t=16 fs and (b) t=32 fs. Bottom: (c) and (d) are the corresponding results for l=10 μm. The dashed white lines indicate the initial target profile and the nominal focused intensity (without plasma) is 10^{21} Wcm^{-2} in both cases.

rameters provides the following first order approximate relationship for the $2\omega_L$ conversion efficiency $\eta_{2\omega_L}$:

$$\eta_{2\omega_L} \propto |E_X(d/2)|Abs_L(l)K_{in}(d) \qquad (4)$$

The variation of this relation with d and l is plotted in figure 4(d). This matches well with the simulation results shown in figure 3. This simple model is useful only to demonstrate the trend of the conversion efficiency behaviour. Factors such as relativistic transparency and the re-absorption of $2\omega_L$ generated light are not included. Relativistic transparency will only affect the thinnest targets and the highest intensity pulses and the re-absorption of $2\omega_L$ will only become significant for very thick targets.

C. 3D Simulations

As harmonic light from the plasma aperture can be produced in non-symmetric modes[36,37], it is necessary to extend the investigation to include 3D simulations. Due to the substantial increase in computational requirements involved, a reduced set of simulations were performed to check if the efficiency dependencies observed in 2D are the same in 3D. The results are presented in figure 5(a). The overall trends in the dependencies on l and d are similar to the 2D results, noting that the maximum conversion efficiency is reduced to ~3.5% and the optimal d is found to be slightly larger at (3±0.5) μm (compared to 2μm for 2D). The reduction in conversion efficiency is likely due to the fact that in 2D the intensity is only simulated in the plane of the laser polarisation where the polarisation vector is perfectly normal to the aperture surface. In 3D, there is no significant interaction when the polarisation vector is parallel to the aperture surface, resulting in proportionally less energy available to produce $2\omega_L$ light. The additional degree of freedom also means that the accelerated electrons are less confined to the laser field as they propagate. The total area of the laser focus, as well as the area of the aperture, needs to be considered in 3D, which modifies equation 3 as follows:

$$K_{in}(d) = \int_{-\pi}^{\pi}\int_{0}^{d/2} e^{-(\frac{2\sqrt{ln(2)}r}{\phi_L})^2} r dr d\phi \qquad (5)$$

where the integral is given in cylindrical coordinates. Figure 5(b) shows the calculated $\eta_{2\omega_L}$ using equation 3 to account for the changes in 3D. This results in an increase of the optimal d by ~0.5 μm.

To directly compare the dependencies of $\eta_{2\omega_L}$ on d and l in 2D and 3D, line-outs from both sets of simulation results are presented in figure 5(c) for a fixed l=10 μm and figure 5(d) for a fixed d=2 μm in 2D and d=3 μm in 3D (i.e. the optimum diameter in each case). The model calculations based on the approximate conversion relations are also shown for the 2D and 3D cases, and are found to be in good overall agreement with the trends observed in the simulation results.

The 2D and 3D simulation results exhibit similar overall trends. The efficiency increases rapidly with d to an optimum value, and as the aperture size is increased beyond this, $\eta_{2\omega_L}$ decreases more slowly with d in the 3D case. The optimum d is also ~0.5 μm higher in 3D, as predicted by the simple model. As l is varied (for the optimal d) the efficiency rises slightly faster in the 3D case compared to the corresponding results in 2D, before saturating at ~3.5%. These discrepancies may be due to the optimal d being slightly bigger in the 3D case. As the laser pulse expands after focus, the intensity decreases with r^2 in 3D, compared to r in 2D, which will change the effective intensity. Second-order effects such as self-focusing[42,43] and reflection of the laser pulse as it moves through the aperture may also induce discrepancies between the 2D and 3D, as these process can change the intensity and longitudinal electric field.

Figure 6 presents the laser intensity profile of the drive laser pulse in two example targets, with differing l, to illustrate the self-focusing and scalloping behaviour in the plasma aperture. Figure 6(a) and (b) shows the ω_L intensity profile, in the $X-Y$ plane along Z=0 μm from the 3D simulations for l=0.5 μm, at example times t=16 fs and t=32 fs, respectively. The laser pulse is observed to experience self-focusing as it passes through the aperture to a position of X ≈2.5 μm before expanding out into free-space. Note that the intensity increases from the nominal intensity of 1×10^{21} Wcm^{-2} (without plasma) to ~4×10^{21} Wcm^{-2}. This is a factor of two higher than can be achieved with the same focus in the 2D simulations due to dimensionality effects (the pulse energy can only be focused in a plane in 2D and focuses radially in 3D).

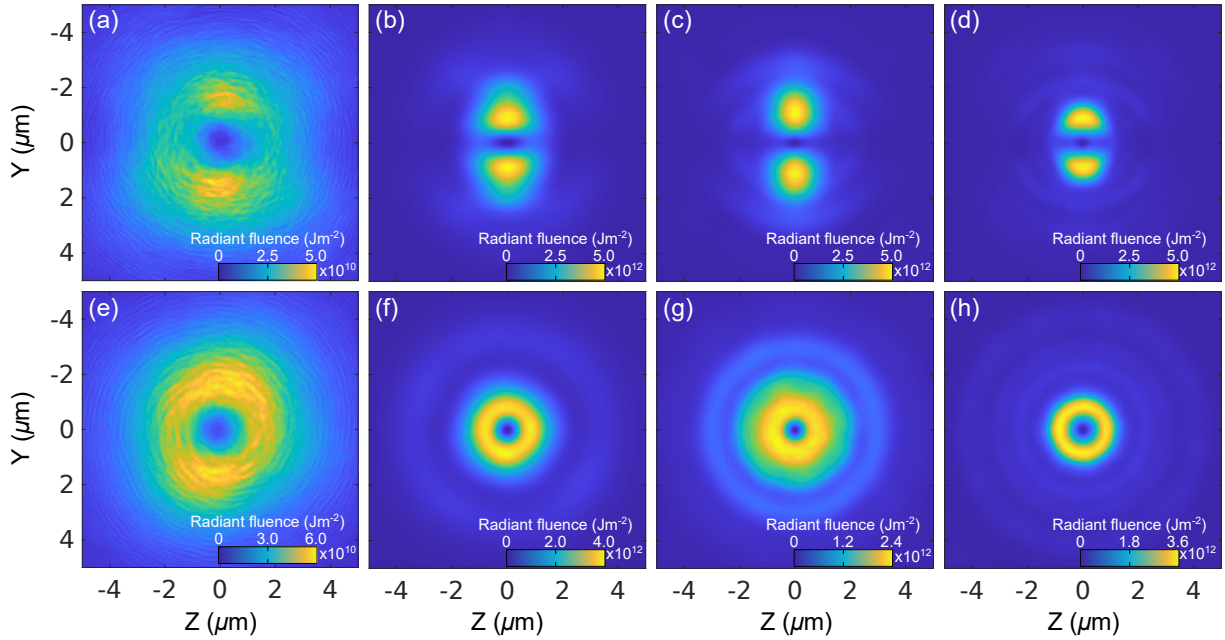

FIG. 7. Time-integrated spatial mode structure 5 μm from the rear of the target. Top: linear polarisation and (a) d=1 μm, (b) d=2 μm, (c) d=3 μm and (a) d=4 μm, all with l=6 μm. Bottom: Corresponding results with circular polarisation, for otherwise same laser and target parameters.

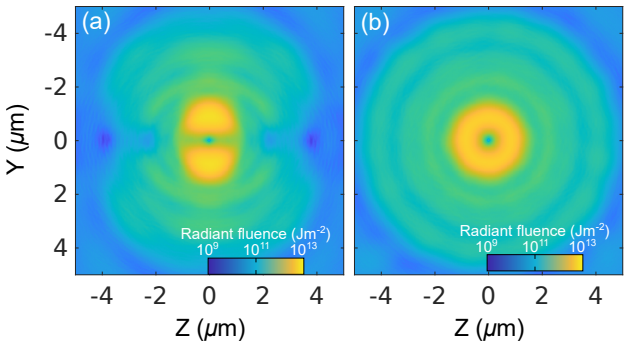

FIG. 8. Time-integrated spatial mode structure 5 μm from the rear of the target with d=4 μm, for (a) linear polarisation, and (b) circular polarisation. Same data as in figure 7(d) and (h), respectively, with fluence plotted on a log scale to show the higher order spatial structures present at larger radii.

When l is increased to 10 μm, as shown for the same example times in figure 6(c) and (d), the self-focusing behaviour is very similar, but the expansion is inhibited by the extended aperture/channel in this case, resulting in scalloping behaviour. At the later time step (figure 6(d)), the pulse is observed to have refocused towards the rear side of the target.

The spatial structure of the generated $2\omega_L$ light in the 3D simulations takes the form of a TEM_{01} mode. The exact spatial distribution of the mode depends on the aperture geometry. Figure 7(a)-(d) shows the change in the mode structure as d is increased for fixed l=6 μm. This is temporally integrated over the full pulse duration. For the smallest aperture (d=1 μm), there is low levels of $2\omega_L$ light generated (note the change in fluence scale) but the TEM_{01} mode is still observed. As d is increased, the mode structure becomes very clear and the overall beam size is observed to reduce. There is also low amounts of $2\omega_L$ light produced outside of this central mode, with even higher order structures, as the aperture size is increased. This is caused by the interference of the generated light varying as the sources are moved further apart[37]. These can be more readily observed on a log-scale, as shown in figure 8(a).

D. Polarisation effects

All the simulation results discussed thus far involve linear polarisation. When the drive laser pulse is circularly polarised, high harmonic light is produced with a Laguerre-Gaussian (LG) mode structure[37]. To explore the effect of polarisation on the $2\omega_L$ conversion efficiency, a further subset of simulations were also performed, for circularly polarised drive laser light. In this case, the peak intensity was halved in order to maintain the same pulse energy as the linear pulse case.

Figures 5(c) and (d) show the conversion efficiency as a function of d and l with circular polarisation for the same fixed parameters as the linear cases. The overall trends are similar to the linear polarisation cases, but with a general increase in overall efficiency in conversion to $2\omega_L$ light. This is due to the polarisation vector always being

normal to the aperture circumference in the case of circular polarisation, resulting in $2\omega_L$ light being produced over the entire wave period.

Figures 7(e)-(h) show the variation in spatial distribution of the temporally integrated $2\omega_L$ light for circular polarisation as d is varied. The generated mode takes the form of a ring distribution[37], as expected from a LG mode. Similar to the linear polarisation case, the aperture diameter affects the size of the main central ring and low-level higher order ring-like distributions are evident as separation of the electron bunches increases (i.e. with increasing d), resulting in a change to the interference pattern. This is more clearly observed on the log-scale in figure 8(b).

E. Effects of temporal intensity contrast

In practice, depending on the temporal-intensity contrast of the laser pulse, some degree of ionisation and expansion of the target may be induced early in the interaction, prior to the arrival of the main pulse. There are various techniques that can be applied to improve the contrast of the pulse, including the use of plasma mirrors[15–17], but depending on the final intensity profile of the leading edge of the laser pulse, preplasma may still be generated, resulting in an expansion of plasma towards the centre of the aperture. This will result in a reduction of the effective aperture diameter as the critical surface moves inwards, such that the $2\omega_L$ light generation will take the characteristics of that produced by a smaller aperture target.

The rising edge of the laser may also produce a degree of underdense plasma within the aperture, which may affect propagation of the laser pulse. To test the impact of this, a series of 3D simulations was conducted, in which the inside of a $d = 3\mu$m, $l = 6\mu$m aperture target was filled with plasma of varying density. The influence this has on the conversion efficiency to $2\omega_L$ light is shown in figure 9(a). For densities less than $0.1n_{crit}$, there is very little (a few percent) reduction in conversion efficiency. The reduction is more significant at higher densities ($\sim$60% at n_{crit}), but it is not expected that the targets would be used under the low temporal-intensity contrast conditions that would induce such a closure of the aperture. A fuller investigation of this requires 3D magnetohydrodynamical simulations, which is outside the scope of this work.

F. Effects of tapering the aperture

The results presented so far involve targets for which the entrance and exit apertures are the same size, creating a parallel channel in cases with a large thickness-to-diameter ratio. It is possible to further optimise the $2\omega_L$ light generation by shaping the target geometry to control the self-focusing of the laser pulse. An additional series of 3D simulations were run, in which the walls of the channel created within the aperture were angled (forming a conical target) by defining different entrance and exit diameters, d_1 and d_2, respectively. Figure 9(b) shows the conversion efficiency to $2\omega_L$ light as a function of d_1, for fixed l=6 μm and d_2=2 μm. The conversion efficiency is improved by increasing the size of the entrance diameter, reaching a maximum of $\sim$6.9% for an optimum d_1=8 μm. The optimum occurs when the convergence angle of the laser undergoing self-focusing matches the angle of the cone walls. This can be readily observed when comparing figures 9(c) and (d). For the case d_1= 3μm (figure 9(c)) self-focusing of the propagating light results in a focal position inside the target, similar to 6(c). For d_1=8 μm, the propagating laser light self-focuses close to the exit aperture. For higher d_1, the focal position moves increasingly beyond the exit aperture and the laser pulse interacts with a shorter length of plasma wall, as the laser pulse needs to propagate deep within the aperture before interacting with it. It may be possible to further tailor geometry of these targets to improve the conversion efficiency and the optimum may also depend on the temporal-intensity contrast of the laser pulse.

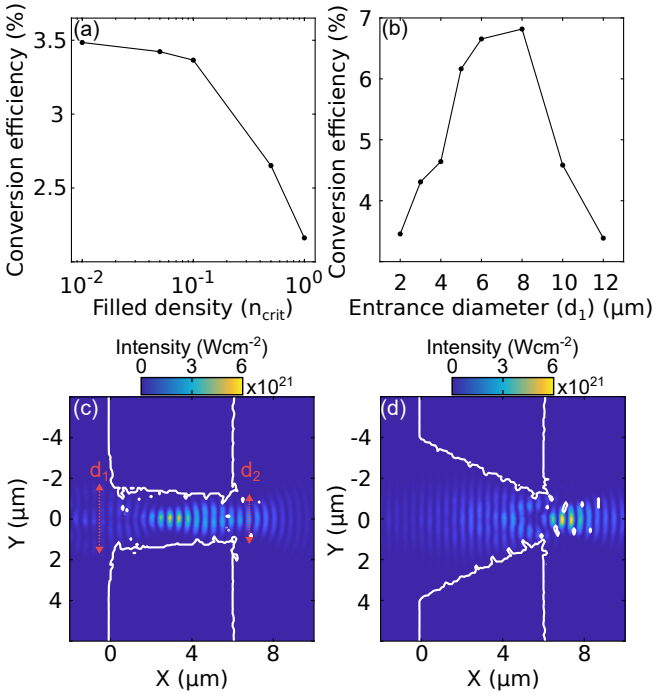

FIG. 9. (a) Conversion efficiency to $2\omega_L$ light as a function of the plasma density within the aperture, for a d=2 μm, $L = 6$ μm target. (b) Conversion efficiency to $2\omega_L$ as a function of the entrance diameters d_1, for a fixed exit diameter d_2=2 μm and l=6 μm. (c) Intensity profile of the drive laser light in the $X - Y$ plane at Z=0 μm, from 3D simulations, for d_1=3 μm (d_2=2 μm and l=6 μm) at t=23. (d) Same, for d_1=8 μm.

IV. SUMMARY

Following our previous work on the self-generation of a relativistic plasma aperture during the interaction of intense laser light with an ultrathin foil[33], and the resultant harmonic generation in higher order spatial modes[36], we have performed a numerical investigation to explore the use of a preformed plasma aperture to achieve a similar output in a more simplified target. The results demonstrate that incoming laser light in a fundamental TEM_{00} mode is converted to relativistically-intense second harmonic radiation emission in higher order modes. The efficiency of conversion is explored as a function of aperture diameter and target thickness and it is found that there exists an optimal diameter that results in a saturation of conversion efficiency as the thickness is increased. This is shown to be proportional to the intensity of light that can enter the aperture, the strength of the longitudinal electric field at the aperture circumference and the absorption of the laser energy. This study was performed for linear polarisation, in both 2D and 3D, which overall exhibit the same trends, allowing computationally efficient 2D simulations to more readily explore a multi-dimensional parameter space. Extension to circular polarisation in 3D produces broadly similar trends in conversion efficiency.

The optimum target conditions for generation of a TEM_{01} mode of $2\omega_L$ light, for the parameter range explored, yielded a conversion efficiency of $\sim$6.9%, while the optimal efficiency for the generation of a $2\omega_L$ LG mode was found to be $\sim$4%. There is potential for this to be increased further by tuning the profile of the tapered targets. As the intensity of the input pulse is increased, the efficiency is reduced slightly, but conversion efficiency on this order still produces $2\omega_L$ light intense enough to induce highly relativistic plasma oscillations. It has also been shown that there is scope for tuning the size of the mode structure and the mode order by variation of the aperture diameter. This demonstrates that a preformed aperture target irradiated by an intense laser pulse can function as a plasma optical device for the generation of $2\omega_L$ light with spatial mode structure that can be changed from non-OAM to OAM by variation of the drive laser polarisation.

This work is financially supported by EPSRC (grant numbers EP/R006202/1 and EP/V049232/1) and STFC (grant number ST/V001612/1). It used the ARCHIE-WeSt and ARCHER2 high performance computers, with access to the latter provided via the Plasma Physics HEC Consortia (EP/R029148/1), and the University of Cambridge Research Computing Service (funded by Grant No. EP/P020259/1). EPOCH was developed under EPSRC grant EP/G054940/1. The research has also received funding from Laserlab-Europe (grant agreement no. 871124, European Union's Horizon 2020 research and innovation programme).

DATA AVAILABILITY STATEMENT

Data associated with research published in this paper can be accessed at https://doi.org/10.15129/823f848a-bb9c-4f84-a883-86911435f8d3

AUTHOR DECLARATIONS

The authors have no conflicts to disclose.

[1]G. A. Mourou, T. Tajima, and S. V. Bulanov, "Optics in the relativistic regime," Reviews of modern physics **78**, 309 (2006).
[2]H. Daido, M. Nishiuchi, and A. S. Pirozhkov, "Review of laser-driven ion sources and their applications," Reports on progress in physics **75**, 056401 (2012).
[3]A. Macchi, M. Borghesi, and M. Passoni, "Ion acceleration by superintense laser-plasma interaction," Reviews of Modern Physics **85**, 751 (2013).
[4]S. V. Bulanov, T. Z. Esirkepov, V. S. Khoroshkov, A. V. Kuznetsov, and F. Pegoraro, "Oncological hadrontherapy with laser ion accelerators," Physics Letters A **299**, 240–247 (2002).
[5]K. Zeil, M. Baumann, E. Beyreuther, T. Burris-Mog, T. E. Cowan, W. Enghardt, L. Karsch, S. D. Kraft, L. Laschinsky, J. Metzkes, *et al.*, "Dose-controlled irradiation of cancer cells with laser-accelerated proton pulses," Applied Physics B **110**, 437–444 (2013).
[6]F. Kroll, F.-E. Brack, C. Bernert, S. Bock, E. Bodenstein, K. Brüchner, T. E. Cowan, L. Gaus, R. Gebhardt, U. Helbig, *et al.*, "Tumour irradiation in mice with a laser-accelerated proton beam," Nature Physics **18**, 316–322 (2022).
[7]M. Borghesi, A. Bigongiari, S. Kar, A. Macchi, L. Romagnani, P. Audebert, J. Fuchs, T. Toncian, O. Willi, S. Bulanov, *et al.*, "Laser-driven proton acceleration: source optimization and radiographic applications," Plasma Physics and Controlled Fusion **50**, 124040 (2008).
[8]M. Barberio, M. Scisciò, S. Vallières, F. Cardelli, S. N. Chen, G. Famulari, T. Gangolf, G. Revet, A. Schiavi, M. Senzacqua, *et al.*, "Laser-accelerated particle beams for stress testing of materials," Nature Communications **9**, 1–7 (2018).
[9]M. Roth, T. E. Cowan, M. H. Key, S. P. Hatchett, C. Brown, W. Fountain, J. Johnson, D. M. Pennington, R. A. Snavely, S. C. Wilks, *et al.*, "Fast ignition by intense laser-accelerated proton beams," Physical Review Letters **86**, 436 (2001).
[10]J. C. Fernández, B. J. Albright, F. N. Beg, M. E. Foord, B. M. Hegelich, J. J. Honrubia, M. Roth, R. B. Stephens, and L. Yin, "Fast ignition with laser-driven proton and ion beams," Nuclear Fusion **54**, 054006 (2014).
[11]E. Cormier-Michel, E. Esarey, C. G. R. Geddes, C. B. Schroeder, K. Paul, P. J. Mullowney, J. R. Cary, and W. P. Leemans, "Control of focusing fields in laser-plasma accelerators using higher-order modes," Physical Review Special Topics-Accelerators and Beams **14**, 031303 (2011).
[12]J. Vieira and J. Mendonça, "Nonlinear laser driven donut wakefields for positron and electron acceleration," Physical Review Letters **112**, 215001 (2014).
[13]J. Vieira, J. T. Mendonça, and F. Quéré, "Optical control of the topology of laser-plasma accelerators," Physical Review Letters **121**, 054801 (2018).
[14]J. W. Wang, C. B. Schroeder, R. Li, M. Zepf, and S. G. Rykovanov, "Plasma channel undulator excited by high-order laser modes," Scientific Reports **7**, 1–12 (2017).
[15]U. Teubner, U. Wagner, and E. Förster, "Sub-10 fs gating of optical pulses," Journal of Physics B: Atomic, Molecular and Optical Physics **34**, 2993 (2001).
[16]B. Dromey, S. Kar, M. Zepf, and P. Foster, "The plasma mirror—a subpicosecond optical switch for ultrahigh power lasers," Review of Scientific Instruments **75**, 645–649 (2004).

[17]G. Doumy, F. Quéré, O. Gobert, M. Perdrix, P. Martin, P. Audebert, J. C. Gauthier, J.-P. Geindre, and T. Wittmann, "Complete characterization of a plasma mirror for the production of high-contrast ultraintense laser pulses," Physical Review E **69**, 026402 (2004).

[18]M. Nakatsutsumi, A. Kon, S. Buffechoux, P. Audebert, J. Fuchs, and R. Kodama, "Fast focusing of short-pulse lasers by innovative plasma optics toward extreme intensity," Optics Letters **35**, 2314–2316 (2010).

[19]R. Wilson, M. King, R. J. Gray, D. C. Carroll, R. J. Dance, C. Armstrong, S. J. Hawkes, R. J. Clarke, D. J. Robertson, D. Neely, *et al.*, "Ellipsoidal plasma mirror focusing of high power laser pulses to ultra-high intensities," Physics of Plasmas **23**, 033106 (2016).

[20]R. Wilson, M. King, R. J. Gray, D. C. Carroll, R. J. Dance, N. M. H. Butler, C. Armstrong, S. J. Hawkes, R. J. Clarke, D. J. Robertson, *et al.*, "Development of focusing plasma mirrors for ultraintense laser-driven particle and radiation sources," Quantum Beam Science **2**, 1 (2018).

[21]J. Ren, W. Cheng, S. Li, and S. Suckewer, "A new method for generating ultraintense and ultrashort laser pulses," Nature Physics **3**, 732–736 (2007).

[22]R. Lichters, J. Meyer-ter Vehn, and A. Pukhov, "Short-pulse laser harmonics from oscillating plasma surfaces driven at relativistic intensity," Physics of Plasmas **3**, 3425–3437 (1996).

[23]A. Tarasevitch, A. Orisch, D. von der Linde, P. Balcou, G. Rey, J.-P. Chambaret, U. Teubner, D. Klöpfel, and W. Theobald, "Generation of high-order spatially coherent harmonics from solid targets by femtosecond laser pulses," Physical Review A **62**, 023816 (2000).

[24]U. Teubner, K. Eidmann, U. Wagner, U. Andiel, F. Pisani, G. D. Tsakiris, K. Witte, J. Meyer-ter Vehn, T. Schlegel, and E. Förster, "Harmonic emission from the rear side of thin overdense foils irradiated with intense ultrashort laser pulses," Physical Review Letters **92**, 185001 (2004).

[25]G. Shvets, N. J. Fisch, A. Pukhov, and J. Meyer-ter Vehn, "Superradiant amplification of an ultrashort laser pulse in a plasma by a counterpropagating pump," Physical Review Letters **81**, 4879 (1998).

[26]V. M. Malkin, G. Shvets, and N. J. Fisch, "Fast compression of laser beams to highly overcritical powers," Physical Review Letters **82**, 4448 (1999).

[27]R. M. G. M. Trines, F. Fiuza, R. Bingham, R. A. Fonseca, L. O. Silva, R. A. Cairns, and P. A. Norreys, "Simulations of efficient raman amplification into the multipetawatt regime," Nature Physics **7**, 87–92 (2011).

[28]S. Monchocé, S. Kahaly, A. Leblanc, L. Videau, P. Combis, F. Réau, D. Garzella, P. D'Oliveira, P. Martin, and F. Quéré, "Optically controlled solid-density transient plasma gratings," Physical Review Letters **112**, 145008 (2014).

[29]Q. Chen, D. Maslarova, J. Wang, S. X. Lee, V. Hornỳ, and D. Umstadter, "Transient relativistic plasma grating to tailor high-power laser fields, wakefield plasma waves, and electron injection," Physical Review Letters **128**, 164801 (2022).

[30]H.-C. Wu, Z.-M. Sheng, Q.-J. Zhang, Y. Cang, and J. Zhang, "Manipulating ultrashort intense laser pulses by plasma bragg gratings," Physics of plasmas **12**, 113103 (2005).

[31]M. R. Edwards, V. R. Munirov, A. Singh, N. M. Fasano, E. Kur, N. Lemos, J. M. Mikhailova, J. S. Wurtele, and P. Michel, "Holographic plasma lenses," Physical Review Letters **128**, 065003 (2022).

[32]Z.-M. Sheng, K. Mima, J. Zhang, and H. Sanuki, "Emission of electromagnetic pulses from laser wakefields through linear mode conversion," Physical Review Letters **94**, 095003 (2005).

[33]B. Gonzalez-Izquierdo, R. J. Gray, M. King, R. J. Dance, R. Wilson, J. McCreadie, N. M. Butler, R. Capdessus, S. Hawkes, J. S. Green, *et al.*, "Optically controlled dense current structures driven by relativistic plasma aperture-induced diffraction," Nature Physics **12**, 505–512 (2016).

[34]B. Gonzalez-Izquierdo, M. King, R. J. Gray, R. Wilson, R. J. Dance, H. Powell, D. A. Maclellan, J. McCreadie, N. M. Butler, S. Hawkes, *et al.*, "Towards optical polarization control of laser-driven proton acceleration in foils undergoing relativistic transparency," Nature Communications **7**, 1–10 (2016).

[35]V. A. Vshivkov, N. M. Naumova, F. Pegoraro, and S. V. Bulanov, "Nonlinear electrodynamics of the interaction of ultra-intense laser pulses with a thin foil," Physics of Plasmas **5**, 2727–2741 (1998).

[36]M. J. Duff, R. Wilson, M. King, B. Gonzalez-Izquierdo, A. Higginson, S. D. R. Williamson, Z. E. Davidson, R. Capdessus, N. Booth, S. Hawkes, D. Neely, R. E. Gray, and P. McKenna, "High order mode structure of intense light fields generated via a laser-driven relativistic plasma aperture," Scientific Reports **10**, 1–10 (2020).

[37]L. Yi, "High-harmonic generation and spin-orbit interaction of light in a relativistic oscillating window," Physical Review Letters **126**, 134801 (2021).

[38]T. D. Arber, K. Bennett, C. S. Brady, A. Lawrence-Douglas, M. G. Ramsay, N. J. Sircombe, P. Gillies, R. G. Evans, H. Schmitz, A. R. Bell, and C. P. Ridgers, "Contemporary particle-in-cell approach to laser-plasma modelling," Plasma Phys. Control. Fusion. **57**, 113001 (2015).

[39]E. J. Dolier, M. King, R. Wilson, R. J. Gray, and P. McKenna, "Multi-parameter bayesian optimization of laser-driven ion acceleration in particle-in-cell simulations," New Journal of Physics (Submitted).

[40]R. A. Snavely, M. H. Key, S. P. Hatchett, T. E. Cowan, M. Roth, T. W. Phillips, M. A. Stoyer, E. A. Henry, T. C. Sangster, M. S. Singh, *et al.*, "Intense high-energy proton beams from petawatt-laser irradiation of solids," Physical Review Letters **85**, 2945 (2000).

[41]S. C. Wilks, A. B. Langdon, T. E. Cowan, M. Roth, M. Singh, S. Hatchett, M. H. Key, D. Pennington, A. MacKinnon, and R. A. Snavely, "Energetic proton generation in ultra-intense laser–solid interactions," Physics of Plasmas **8**, 542–549 (2001).

[42]M. Siegrist, "Self-focusing in a plasma due to ponderomotive forces and relativistic effects," Optics Communications **16**, 402–407 (1976).

[43]T. Frazer, R. Wilson, M. King, N. Butler, D. Carroll, M. Duff, A. Higginson, J. Jarrett, Z. Davidson, C. Armstrong, *et al.*, "Enhanced laser intensity and ion acceleration due to self-focusing in relativistically transparent ultrathin targets," Physical Review Research **2**, 042015 (2020).